

# Granular Resistive Force Theory Implementation for Three-Dimensional Trajectories

Laura Treers, Cyndia Cao, and Hannah S. Stuart

**Abstract**—Modelling interaction forces as bodies intrude into granular media is a longstanding challenge in the design and control of machines that navigate and manipulate these highly complex materials. Granular Resistive Force Theory, or RFT, is a flexible, reduced-order model for predicting intrusion forces on bodies in granular media. 2D RFT describes the forces on a plate whose velocity and normal vectors lie in the same vertical plane. We introduce a 3D RFT method that projects the total velocity vector into two scenarios that can already be described by 2D RFT, which allows us to extend the model into 3D with minimal additional experimental characterization. We then superimpose these independently calculated forces, weighted by experimentally fit scaling factors, to determine the total force on the plate. When applied to discretized convex hulls, this method performs force estimates of arbitrary trajectories in 3D space. The proposed formulation predicts forces experienced by oscillating and circumnating bodies, motions motivated by mole crab burrowing and plant root growth respectively. This method is well-suited to complement more complex computational tools, such as Discrete Element Method. By expanding the application of RFT to 3D scenarios, a broader set of real-world applications can now be analyzed.

**Index Terms**—Dynamics, Contact Modeling, Methods and Tools for Robot System Design

## I. INTRODUCTION

COUNTLESS animal species, such as arthropods, mollusks, plants and annelids, demonstrate amazing burrowing and excavation abilities with complex three-dimensional morphologies and behaviors. Robotic applications mimic biological mechanisms in order to penetrate [1]–[3] and locomote [4]–[6] in granular media. However, they have yet to match the ability of these organisms to manipulate granular media and traverse underground with such dexterity. Potential uses for these types of machines include geotechnical and agricultural site characterization [7], remote exploration of sandy planets, manipulation of manufacturing materials, construction and excavation, and the development of biophysical models [8]–[11]. Understanding interaction forces between machines and

granular media through predictive simulations can streamline both mechanism design and control.

### A. Background

Resistive force theory (RFT) – a general method utilized for over 50 years [12], [13] – models interaction forces using lumped empirical parameters in lieu of a constitutive model or contact law. In 2009, a simplified RFT was developed for dry, uniform granular materials in horizontal motion planes, and it was demonstrated that resistive forces, i.e. forces imparted by the substrate that oppose motion, scale with cross-sectional area and are largely independent of intrusion speed at low speeds [5]. Further studies demonstrated that similar principles hold in other planes of motion [14], [15]. RFT in three-dimensional (3D) space is defined as [15]:

$$\mathbf{F} = \int ds [f_{\perp}(\mathbf{v}, \hat{\mathbf{t}})\hat{\mathbf{n}} + f_{\parallel}(\mathbf{v}, \hat{\mathbf{t}})\hat{\mathbf{t}}] \quad (1)$$

where  $f_{\perp}$  and  $f_{\parallel}$  are scaling factors,  $\mathbf{v}$  is the element velocity direction, and  $\hat{\mathbf{t}}$  and  $\hat{\mathbf{n}}$  are the tangent direction and normal direction vectors of the element.

In practice, granular RFT typically utilizes penetrometry tests across various substrate types, intruder plate orientations, and intruder plate trajectories in order to characterize lumped substrate properties. Eqn. 1 is often simplified to planar or specialized trajectories in order to reduce the experimental parameter space. In the horizontal planar formulation [15], [16], changes in penetration depth are not considered. In the vertical planar formulation [14], [17], the plate element's motion must lie in the vertical plane that contains its surface normal. *We present a closed-form method of implementing granular RFT in 3D using penetrometry data gathered from only these two horizontal and vertical planes, with the goal of streamlining resistive lumped-parameter identification.*

The desire to apply 3D granular RFT to engineering applications continues to grow. For a legged robot that walks on extruded C-legs, Li et. al (2013) used RFT to predict the leg curvature and rotation velocity that would produce the fastest forward motion. However, this 2D RFT characterization is insufficient to fully describe the force response of an arbitrary 3D body and motion, such as the complex leg motions of the zebra-tailed lizard [18]. Research in the design of excavators for unmanned construction systems has utilized an “improved RFT” (or i-RFT) to model interaction mechanics with a 3D bucket [19].<sup>1</sup> A 2020 study on rover design and control applied

Manuscript received: October, 15, 2020; Revised January, 9, 2021; Accepted January, 15, 2021. This paper was recommended for publication by Editor Lucia Pallottino upon evaluation of the Associate Editor and Reviewers' comments. This work was supported by and carried out at the University of California at Berkeley. L. Treers is supported by a National Defense Science and Engineering Graduate Fellowship through the Office of Naval Research and a Berkeley Graduate Fellowship. C. Cao is supported by a NASA Space Technology Research Fellowship 80NSSC19K1167. This work was supported by an Early Career Faculty grant (80NSSC21K0069) from NASA's Space Technology Research Grants Program.

L. Treers, C. Cao and H.S. Stuart are with College of Engineering, Mechanical Engineering Department, University of California at Berkeley, CA USA ltrees@berkeley.edu

Digital Object Identifier (DOI): see top of this page.

<sup>1</sup>The “i-RFT” model introduced by Tsuchiya et al. incorporates a correction factor into the intrusion angle definition, which accounts for the angle of the slope surface to better take into consideration surface mounding effects.

a “quasi-3D RFT” to analyze forces on rover wheels sweeping through granular media [20].<sup>2</sup> These prior methods make physical motion assumptions based on the specific application such that they are ill-suited to other bodies and motions. Our proposed method does not assume such constraints.

RFT only predicts forces on the intruder and cannot predict behavior within the granular material itself. This is opposed to the Discrete Element Method (or DEM), which solves the equations of motion for every particle [21]–[24], and the Material Point Method (MPM) which treats the substrate as a continuum with a frictional yield criterion and plastic flow [25], [26]. As such, granular RFT is subject to several limitations. It does not account for localized jamming or unpacking due to concave body geometries or substrate fluidization, and it assumes relatively flat, homogeneous dry granular media. In high-velocity scenarios (approximately  $>0.2$  m/s), inertial effects of the granular particles are non-negligible and a “Dynamic RFT” formulation can be implemented [17]; however, the implementation we introduce in this paper is performed with relatively slow motions ( $\leq 2.5$  cm/s).

Despite these limitations, RFT’s low computational cost makes it desirable for applications which benefit from fast, high-level understanding of interaction forces and force distributions. Depending on processing power and model simplification, DEM and MPM simulation times can range from an hour to several days or weeks, while RFT force calculations have the potential to be computed in real time, depending on the chosen spatial and temporal resolution. While RFT lacks the high precision of DEM or MPM, it presents a good approximation when speed is paramount. Therefore, RFT is ideal for prototyping or performing initial studies before investing more time into DEM or MPM analysis or building a physical device. RFT is especially useful in narrowing large parameter spaces to expedite the process of mechanism and controller design.

## B. Overview

Fig. 1 conceptualizes the proposed RFT implementation framework. In Section II, we describe a method for estimating the resistive forces on a plate penetrating into sand with any orientation and trajectory via velocity decomposition. Section III describes our experimental testbeds and procedures for testing the efficacy of this method. In Section IV-A, lumped-parameter scaling factors are characterized with a flat plate element moving in the horizontal plane. The proposed RFT method is then validated using a flat plate with various velocity vectors in 3D in Section IV-B.

The principle of RFT superposition allows for the decomposition of a 3D convex body into 2D plate elements [26]. Simulation of convex 3D shapes is performed using our RFT implementation by summing the resistive forces acting on each plate element. The remainder of the results demonstrate how this tool can be applied to curved shapes

<sup>2</sup>Shrivastava, et al. make the assumption that the direction of resistive forces of each element in the horizontal plane are opposite to their velocity vector,  $\mathbf{F}_j = -\mathbf{v}_j$ , stemming from the observation that the velocities of most plate elements on a spinning wheel have directions nearly “in line” with the normal vectors, i.e.  $\mathbf{n}_j \cdot \mathbf{v}_j > 0.5$ .

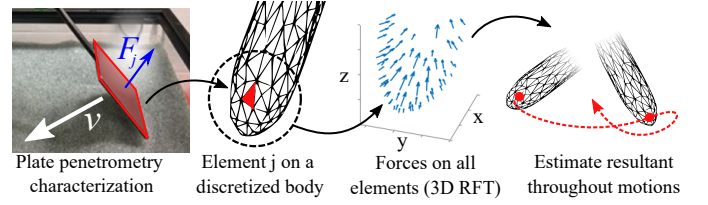


Fig. 1. **Proposed 3D RFT methodology.** A visual representation of the process for estimating intrusion forces using RFT, from planar force characterization to summing the forces on all discretized plate elements on a 3D body throughout its motion.

for analysis of burrowing mechanisms. We test the intrusion of a curved 3D ellipsoid undergoing body pitch oscillation, inspired by motions observed in the Pacific mole crab, in Section IV-C and parametrically simulate circumnutations of a 3D paraboloid during its 3D intrusion trajectory, inspired by plant root behavior [27], in Section IV-D. As discussed in Section V, this tool is well-suited to perform rapid studies to understand robot design and control trends.

## II. 3D RFT METHOD

We build upon previous principles of vertical 2D RFT, which uses two angles ( $\beta, \gamma$ ) to describe the orientation and velocity direction of a plate element, by introducing a third independent angle ( $\psi$ ). A plate element,  $j$ , shown in Fig. 2(A), lies in  $\mathbf{E}_i$ , the Newtonian frame, where  $\mathbf{E}_3$  defines the vertical axis to which gravity forces are aligned. An intermediate basis  $\mathbf{e}_i$  is defined by a simple rotation about  $\mathbf{E}_3$  such that the projection of the plate normal  $\mathbf{n}$  onto the horizontal plane  $\mathbf{E}_1$ – $\mathbf{E}_2$  lies in the  $\mathbf{e}_2$  direction. Thus, the intersection of the plate’s surface and the horizontal plane  $\mathbf{E}_1$ – $\mathbf{E}_2$  aligns with  $\mathbf{e}_1$ . The angle between  $\mathbf{n}$  and  $\mathbf{e}_2$  is parameterized by  $\beta$ . The plate has velocity  $\mathbf{v}$  and is assumed to have no angular velocity. The velocity direction is characterized by parameter  $\psi$ , which is defined as the angle between  $\mathbf{e}_2$  and the projection of  $\mathbf{v}$  onto the horizontal plane  $\mathbf{E}_1$ – $\mathbf{E}_2$ . Plate velocity  $\mathbf{v}$  is decomposed into two components:  $\mathbf{v}_1$  and  $\mathbf{v}_{23}$ . The velocity vector is first projected onto the  $\mathbf{e}_1$  axis to form the component  $\mathbf{v}_1$ . The component  $\mathbf{v}_{23}$  is defined as  $\mathbf{v}_{23} = \mathbf{v} - \mathbf{v}_1$ , which places it in the same vertical plane as the surface normal, denoted as  $\mathbf{e}_{23}$ . The angle between  $\mathbf{v}_{23}$  and  $\mathbf{e}_2$  is defined as  $\gamma$ .

Following this decomposition, 2D RFT is applied in the  $\mathbf{e}_{23}$  plane to produce reference force  $\tilde{\mathbf{F}}_{23}$ , while the term in the  $\mathbf{e}_1$  direction is reference force  $\tilde{\mathbf{F}}_1$ , such that:

$$\tilde{\mathbf{F}}_1 = [\alpha_\gamma(\gamma, \beta) \mathbf{e}_1] |z| \delta A \quad (2)$$

$$\tilde{\mathbf{F}}_{23} = [-\alpha_x(\gamma, \beta) \mathbf{e}_2 + \alpha_z(\gamma, \beta) \mathbf{E}_3] |z| \delta A \quad (3)$$

where  $|z|$  is the depth of the element and  $\delta A$  is the infinitesimal area of the element. The resistive coefficients  $\alpha_x$  and  $\alpha_z$ , which are functions of  $\beta$  and  $\gamma$ , are defined in vertical 2D RFT and empirically characterized [14].<sup>3</sup> We compare two different models for resistive coefficient  $\alpha_\gamma$ :

<sup>3</sup>Note that our definition of the horizontal axis  $\mathbf{e}_2$  is mirrored from 2D RFT, hence the sign change in Eqn. 2.

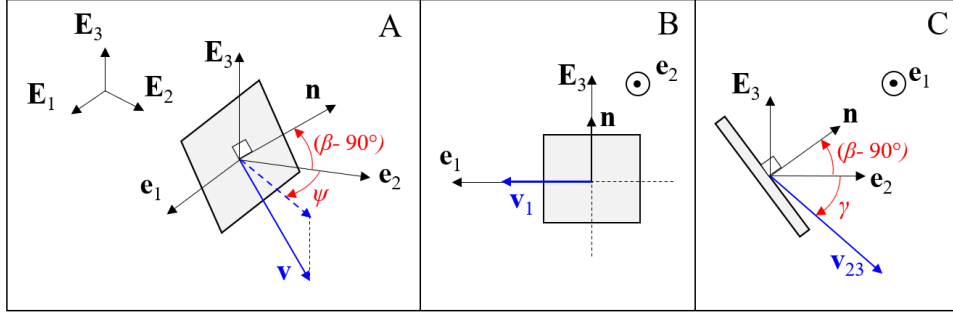


Fig. 2. **3D method angle definitions.** (A) Depiction of plate element coordinate frames and angle definitions in 3D. An example total velocity is indicated, and the dashed blue arrow indicates the projection of total velocity on the horizontal plane. (B) The plate element is viewed along the  $\mathbf{e}_2$  axis, along with the  $\mathbf{v}_1$  component of velocity. (C) The same plate element is viewed along the  $\mathbf{e}_1$  axis, resembling a 2D RFT analysis as presented in [14]. The velocity in this plane,  $\mathbf{v}_{23}$ , is indicated.

- $\alpha_y = \alpha_x(\gamma=0, \beta=0)$  reduces the need for new empirical model fitting for easy adoption.
- A first order approximation of  $\alpha_y(\gamma, \beta)$  yields  $\alpha_y(\beta)$ , and provides more accurate estimates for  $\tilde{\mathbf{F}}_1$  but requires additional experimental characterization data.

The benefit of this decomposition is that it can characterize the scaling effect on 2D RFT that occurs when both components are present, such as when a penetrating object is yawed about the vertical axis. We now introduce dimensionless factors  $f_1$  and  $f_{23}$ , which are functions of  $\psi$  and  $\gamma$ , in order to weight and superimpose the two independent resistive force calculations. We hypothesize that total force experienced by a single plate element  $j$  can be calculated as

$$\mathbf{F}_j = \mathbf{F}_{1,j} + \mathbf{F}_{23,j} = f_1(\psi, \gamma) \tilde{\mathbf{F}}_1 + f_{23}(\psi, \gamma) \tilde{\mathbf{F}}_{23}. \quad (4)$$

When  $\psi = 0^\circ$  and  $\mathbf{v}_1 = 0$ , planar RFT holds such that  $f_1 = 0$  and  $f_{23} = 1$ . Conversely, when  $\psi = 90^\circ$  and  $\mathbf{v}_{23} = 0$ , all motion lies in the  $\mathbf{e}_1$  direction such that  $f_1 = 1$  and  $f_{23} = 0$ . The empirical relationships of  $f_1$  and  $f_{23}$  with intermediate  $\psi$  values are reported in Section IV-A.

The total force on a body is the sum of the resistive forces over all infinitesimal plate elements,  $\mathbf{F} = \sum \mathbf{F}_j$ . We only include the elements which are beneath the substrate surface, i.e.  $\mathbf{F}_j = 0$  if  $z_j > 0$ . We also impose the condition that  $\mathbf{F}_j = 0$  if  $\mathbf{v}_j \cdot \mathbf{n}_j < 0$  in order to remove the effect of elements which are not pushing on the substrate. In past studies utilizing RFT methods, this has been referred to as the “leading edge hypothesis” because only the leading surfaces contribute significantly to the total force [26]. In our formulation the orientation vector  $\mathbf{e}_1$  is not uniquely defined when  $\beta=0^\circ$ . When this occurs,  $\mathbf{e}_1$  is defined as the projection of the element’s total velocity vector onto the  $\mathbf{E}_1$ - $\mathbf{E}_2$  plane. This assumption introduces a discontinuity in the model as  $\beta$  approaches zero, discussed in Section V.

### III. MATERIALS AND METHODS

#### A. Penetrometry experimental setup

A 40 cm x 20 cm x 24 cm tank is filled to approximately 18 cm depth with 0.8 mm glass beads as substrate. Particles are assumed to be approximately spherical and uniform in diameter. A Universal Robot (UR-10) is used to penetrate

different objects into the glass beads with various orientations and trajectories. For plate characterization and validation experiments, square steel plates (5.1cm x 5.1cm x 0.32cm) are fixtured to the load cell, which is located at the end effector of the robot arm. The plate is inserted in the substrate with the velocity vector in the  $\mathbf{E}_2$ - $\mathbf{E}_3$  plane, aligned with the longest edge of the tank. For oscillation and circumnutation experiments, custom rigid bodies are attached, described in detail in sections IV-C and IV-D. For all trials, six-axis force and torque data are obtained from an Axia80 ATI load cell with a sampling rate of 125 Hz. Between each penetration trial, the substrate volume fraction is reset to a loose-packed state by manually stirring the substrate for 5 seconds.<sup>4</sup>

A vertical plate element ( $\beta = 90^\circ$ ) is translated in the horizontal plane at a series of values of  $\psi$  in order to characterize the force scaling relations  $f_1$  and  $f_{23}$ . The force response takes several centimeters of horizontal motion to reach a steady-state plowing behavior, and the mean force in this steady-state region over three trials is utilized for data analysis.

During validation trials, the plate is first yawed by  $\psi$  about  $\mathbf{E}_3$  and then tilted by  $\beta$  about  $\mathbf{e}_1$ . For horizontal trials, steady-state plowing forces are averaged first during each trial, and we compute the mean and standard deviation over three trials. For cases in which there is vertical motion, the peak force value is recorded at maximum depth of insertion. This depth is estimated from the force values in  $\mathbf{e}_2$  and  $\mathbf{E}_3$  achieved in the  $\psi=0$  trial using values of  $\alpha$  from Li et al. [14]; the penetration depths that would produce the measured horizontal and vertical forces are averaged to obtain the predicted depth. This predicted depth is then used to normalize the measured forces across the  $\psi$  values tested. Reported values and standard deviations represent 5 separate penetrometry trials.

#### B. Numerical rigid body simulation structure

A discretized 3D model, e.g., “stereolithography” (STL) format file, is imported into MATLAB for analysis. During simulation, vertices from the STL file in Cartesian coordinate space are indexed and grouped into triangles, using the MATLAB function toolbox *stlread*. The desired trajectory of the

<sup>4</sup>In future work, this process can be made more consistent through the use of a fluidizing bed, as in [15].

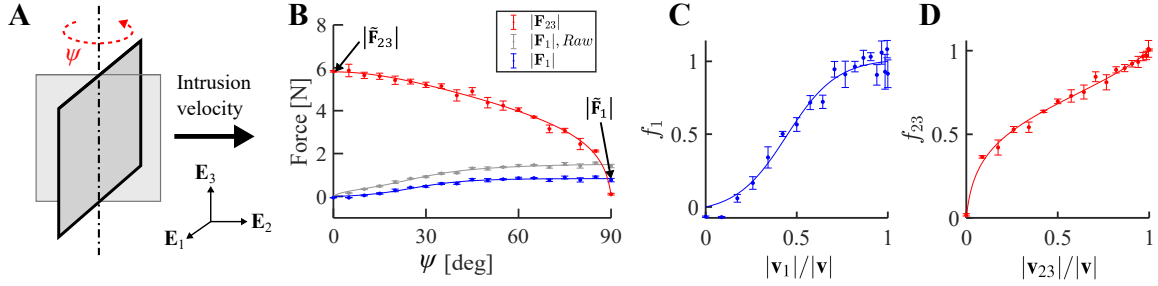


Fig. 3. **Horizontal RFT empirical characterization.** (A) During horizontal characterization,  $\psi$  is varied while  $\beta$  and  $\gamma$  remain constant, where  $\psi = 0^\circ$  when the plate moves in the direction of its surface normal. (B) Measured plate forces when moving in the horizontal plane,  $|\mathbf{F}_1|, Raw$  and  $|\mathbf{F}_{23}|$ , show a nonlinear relationship with  $\psi$ . To compensate for plate thickness, an approximation of force for the thin edge of the plate is subtracted from  $|\mathbf{F}_1|, Raw$  to estimate  $|\mathbf{F}_1|$ . Normalized scaling factors (C)  $f_1$  and (D)  $f_{23}$  accordingly vary as a function of  $|\mathbf{v}_1|/|\mathbf{v}|$  and  $|\mathbf{v}_{23}|/|\mathbf{v}|$ , respectively. Solid curves represent fits to the data using sigmoid functions.

body is specified, including both translational and rotational components in 3D. The position of each triangle center is calculated via a transformation of bases as defined in Fig. 2. Velocity of each triangle center is calculated as

$$\mathbf{v}_j = (\mathbf{r}_{jR} \times \boldsymbol{\omega}) + \mathbf{v}_{COR} \quad (5)$$

where  $\boldsymbol{\omega}$  is the angular velocity of the body about its center of rotation, and  $\mathbf{v}_{COR}$  represents the velocity of the center of rotation of the body.  $\mathbf{r}_{jR}$  represents the position of each triangle center relative to the center of rotation. At each time step of the simulation the parameters  $f_1$ ,  $f_{23}$ ,  $\gamma$ ,  $\beta$ , and  $z$  are calculated at the centroid of each triangle element.

The Fourier coefficients for generic media presented in [14] are utilized to map the calculated  $\beta$  and  $\gamma$  to  $\alpha_x$  and  $\alpha_z$  for a given element. As described by Li et. al, these generic coefficients can be multiplied by a single scaling factor to tune results to a specific granular media. Based on the average of five vertical plate penetration experiments, we calculate the scaling factor for our granular media to be approximately 0.33. The magnitude and direction of force is computed for every discretized element and summed.

#### IV. MODEL CHARACTERIZATION AND VALIDATION

##### A. Horizontal RFT relation for a plate

In order to establish the relationship between the force in  $\mathbf{e}_1$  and  $\mathbf{e}_{23}$  as a function of velocity direction, a set of experiments is performed on a vertically-oriented plate element ( $\beta = 90^\circ$ ) translating in the  $\mathbf{E}_2$  direction at a velocity of 1 cm/s. Because  $\gamma = 0^\circ$ , the  $\mathbf{e}_1$  and  $\mathbf{e}_{23}$  components of velocity change as  $|\mathbf{v}_1|/|\mathbf{v}| = \sin(\psi)$  and  $|\mathbf{v}_{23}|/|\mathbf{v}| = \cos(\psi)$ ; these values can be calculated for arbitrary  $\gamma$  using vector projection. Experimentally, the angle  $\psi$  is varied in increments of  $5^\circ$  while forces are measured. The measured  $|\mathbf{F}_1|, Raw$  component approaches a maximum value of 1.5 N at  $\psi = 90^\circ$ .  $|\mathbf{F}_{23}|$  is comparatively larger over most values of  $\psi$ , with a maximum of 5.8 N at  $\psi = 0^\circ$ , and shows a sharp drop-off at values of  $\psi > 70^\circ$ .

The plate used in this experiment has a non-negligible thickness, which becomes most significant in the  $\mathbf{e}_1$  direction when  $\psi \rightarrow 90^\circ$ . We approximate this effect by applying Eqns. 3 and 4 to estimate  $\mathbf{F}_{23}$  force for the thin edge's face, assuming that its tangential  $\mathbf{F}_1$  component is negligible compared with  $\mathbf{F}_{23}$  of the primary plate's surface. This approximation is subtracted

from the measured force  $|\mathbf{F}_1|, Raw$ , such that the maximum  $|\mathbf{F}_1|$  is 0.9 N, or 60% of  $|\mathbf{F}_1|, Raw$ . Force magnitudes are plotted as a function of  $\psi$  in Fig. 3(B). As  $\psi \rightarrow 90^\circ$ , the reverse face of the plate will also contribute force in  $|\mathbf{F}_1|$ . We currently neglect this reverse-face effect assuming that the shape of  $f_1(\psi, \gamma)$  will not change significantly.

The scaling factor  $f_1$  is defined as the magnitude of  $\mathbf{F}_1$  normalized by its magnitude when  $\mathbf{v} = \mathbf{v}_1$ , i.e.  $|\tilde{\mathbf{F}}_1| = |\mathbf{F}_1(\psi = 90^\circ, \gamma = 0^\circ)|$ . Likewise,  $f_{23}$  is the magnitude of  $\mathbf{F}_{23}$  normalized by its magnitude when  $\mathbf{v} = \mathbf{v}_{23}$ , i.e.  $|\tilde{\mathbf{F}}_{23}| = |\mathbf{F}_{23}(\psi = 0^\circ, \gamma = 0^\circ)|$ . Therefore,  $f_1(\psi, \gamma) = |\mathbf{F}_1(\psi, \gamma = 0^\circ)|/|\tilde{\mathbf{F}}_1|$  and  $f_{23}(\psi, \gamma) = |\mathbf{F}_{23}(\psi, \gamma = 0^\circ)|/|\tilde{\mathbf{F}}_{23}|$ ; these scaling relationships are plotted against normalized velocity components in Fig. 3(C)-(D). The resulting trends are consistent with those found in [16], in which horizontal plate characterization data shows anisotropy. We fit the normalized force data against the normalized velocity with sigmoid functions constrained to the points (0,0) and (1,1). The data follows the form  $|\mathbf{F}_1| = A_1 * \tanh(A_2 * |\mathbf{v}_1|/|\mathbf{v}| - A_3) + A_4$  and  $|\mathbf{F}_{23}| = B_1 * (B_2 * |\mathbf{v}_{23}|/|\mathbf{v}| - B_3) + B_4$ , where  $A_i$  and  $B_i$  are fitting terms. Our fits produced coefficients  $A_1 = 0.44$ ,  $A_2 = 3.62$ ,  $A_3 = 1.61$ ,  $A_4 = 0.41$ ,  $B_1 = 1.99$ ,  $B_2 = 1.61$ ,  $B_3 = 0.97$ , and  $B_4 = 4.31$ .

##### B. Validation using plate elements

In order to test the ability of this 3D granular RFT method to predict insertion forces, plates are translated through granular media in a variety of orientations and insertion angles at a speed of 1 cm/sec. We introduce an alternative velocity parameter  $\phi$  to reflect the constraints of our experimental setup, where  $\phi$  represents the intrusion angle of the total velocity relative to horizontal, and  $\gamma$  can be determined geometrically as depicted in Fig. 4, such that  $\tan(\gamma) = \tan(\phi)/\cos(\psi)$ . The angle  $\psi$  is varied in increments of  $10^\circ$ , from  $0^\circ$  to  $90^\circ$  with three different values of  $\phi$  ( $0^\circ$ ,  $30^\circ$ ,  $60^\circ$ ) and plate angle  $\beta$  ( $30^\circ$ ,  $60^\circ$ , and  $90^\circ$ ). Fig. 5(A) shows the experimental results, alongside the simulation predictions for both proposed models of  $\alpha_\gamma$ . The rods attaching the plate element to the robot end effector, as well as the plate edges, are not taken into account.

Fig. 5(B) depicts the median deviation between the models and average measured force over all tested values of  $\psi$ , plotted for each combination of  $\beta$  and  $\phi$ . Error values are normalized

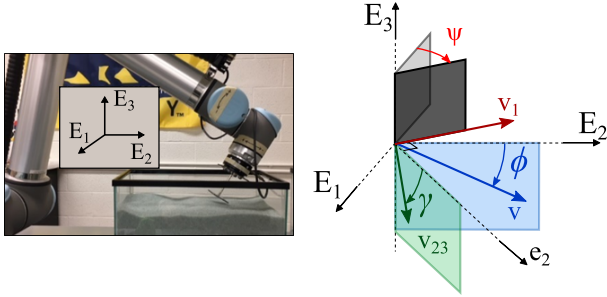


Fig. 4. **Plate validation experiments.** (Left) The experimental setup used for validation experiments consisting of a UR10 robot and plate element attachment, showing the world frame. (Right) During validation experiments, total velocity is fixed in the  $\mathbf{E}_2$ - $\mathbf{E}_3$  plane represented in blue, such that we parameterize it with intrusion angle  $\phi$  in the world frame. The grey plane represents the plate element in the case when  $\beta = 0$  and  $\psi > 0$ . The green plane represents the  $\mathbf{e}_{23}$  plane. Velocity projection  $\mathbf{v}_{23}$  as well as velocity orientation angle  $\gamma$  lie in this plane.

against the total force magnitude predicted at each value of  $\psi$  to present relative error values. Because dividing by the force value at  $\psi = 0^\circ$  or  $90^\circ$  leads to a singularity in some cases, the median value over all values of  $\psi$  is displayed. The median relative error ranges between 1.9 and 34.1 percent for  $|\mathbf{F}_1|$  when  $\alpha_y = \alpha_x(0,0)$ , and between 1.2 and 6.5 percent for  $|\mathbf{F}_1|$  when  $\alpha_y(\beta)$ . The median relative error ranges between 1.5 and 17.2 percent for  $|\mathbf{F}_{23}|$  when  $\alpha_y = \alpha_x(0,0)$ , and between 1.5 and 18.8 percent for  $|\mathbf{F}_{23}|$  when  $\alpha_y(\beta)$ ; the dependence of  $|\mathbf{F}_{23}|$  relative error on  $\alpha_y$  is caused by a change in the total predicted force magnitude. Because there is so little change in  $|\mathbf{F}_{23}|$  error between the two  $\alpha_y$  models, only the case when  $\alpha_y = \alpha_x(0,0)$  is shown.

Error in the  $|\mathbf{F}_1|$  model that arises when using the constant scaling factor  $\alpha_y = \alpha_x(0,0)$  is most pronounced at  $\beta = 90^\circ$  and  $\gamma = \phi = 0^\circ$ ; given that the term  $f_1$  is fit to the data under this condition, the predominant source of this error is  $\alpha_y$  and is alleviated when using  $\alpha_y(\beta)$ .  $|\mathbf{F}_1|$  error for both models is pronounced when  $\psi > 70^\circ$  for  $(\beta=30^\circ, \phi=0^\circ)$  and  $(\beta=60^\circ, \phi=0^\circ)$ , where the experimental data is non-monotonic. Error in  $|\mathbf{F}_{23}|$  is maximized at  $(\phi=60^\circ, \beta=90^\circ)$ . Note that  $\alpha_x$  and  $\alpha_z$  are based on prior work, and not re-characterized on our testbed. Observed errors may be influenced by compliance in the supporting structure of the cantilevered test plate, because these members are thin in order to reduce their resistive forces.

Empirical resistive coefficients  $\alpha_y$  are estimated from the data in Fig. 5(A) using Eqn. 2 and 4, and plotted over  $\beta$  and  $\gamma$  in Fig. 6. Results over  $\beta$  are consolidated by fitting a constant multiplier  $\alpha_y$  to  $|\mathbf{F}_1|$  for each of the  $(\phi, \beta)$  data sets using root mean squared regressions, then averaged for each  $\beta$  value.  $\alpha_y$  more strongly depends on  $\beta$  than  $\gamma$  and the first order approximation of  $\alpha_y(\beta)$  assumes  $\gamma$  to be constant. While less accurate for certain plate element velocities and orientations, assuming  $\alpha_y = \alpha_x(0,0)$  limits the need for additional experimental data sets to characterize. We therefore test the utility of such a simplification for oscillation and circumnutation 3D simulations despite these limitations; these curved shapes will not be dominated by the error-prone regions in  $\mathbf{F}_1$ , and  $|\mathbf{F}_1| < |\mathbf{F}_{23}|$  under a majority of conditions.

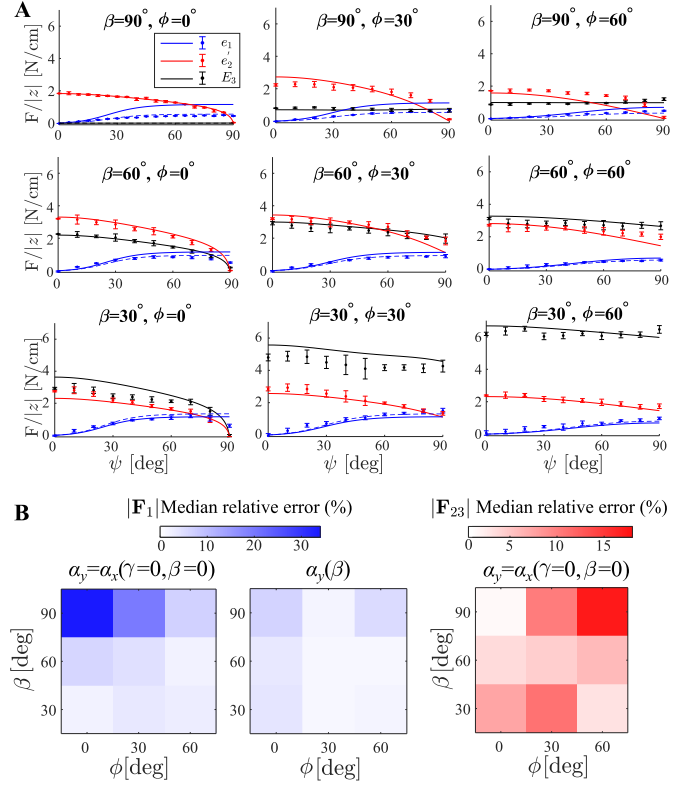


Fig. 5. **Plate validation data.** (A) Representation of results from plate validation experiments for all combinations of  $\beta$  and  $\phi$ . The mean measured force per unit depth from experiments are represented as dots in the  $\mathbf{E}_3$ ,  $\mathbf{e}_2$  and  $\mathbf{e}_1$  directions, and error bars indicate standard deviation. Corresponding model-predicted values are represented as solid lines. The solid blue lines represent model-predicted  $|\mathbf{F}_1|$  force for  $\alpha_y = \alpha_x(0,0)$ , while dashed blue lines represent the results when  $\alpha_y$  is a linear function of  $\beta$ . (B) Median relative error over all values of  $\psi$  for  $|\mathbf{F}_1|$  and  $|\mathbf{F}_{23}|$  – total force along the  $\mathbf{e}_1$  axis, and force in the  $\mathbf{e}_2$ - $\mathbf{E}_3$  plane, respectively – is plotted over  $\beta$  and  $\phi$ . Force values are scaled to the total force magnitude predicted at each value of  $\psi$ .

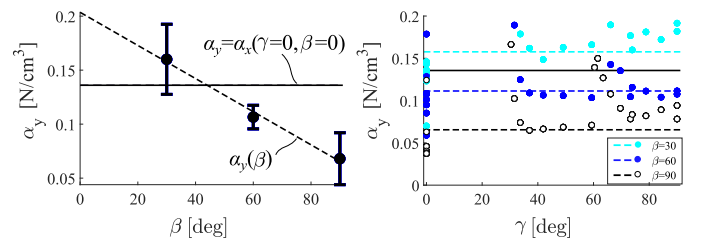


Fig. 6. **Characterization of  $\alpha_y$ .** (Left) The means and standard deviations of fit coefficient  $\alpha_y$  over three values of  $\phi$  are plotted against  $\beta$ . The dashed line indicates a linear fit to the means and solid line represents  $\alpha_y = \alpha_x(0,0)$ . (Right)  $\alpha_y$  coefficients for each individual data point are plotted as a function of  $\gamma$ .  $\alpha_y = \alpha_x(0,0)$  is indicated with a solid black line and dashed colored lines indicate the values of  $\alpha_y$  predicted by the linear fit  $\alpha_y(\beta)$ .

### C. Ellipsoid with body pitch

We simulate a behavior frequently seen in burrowing animals: oscillation in body pitch, as described in [28], [29]. We postulate that oscillation of a body during granular intrusion may provide some advantage during penetration applications. Preliminary experiments, similar to the ones demonstrated in [30], with two mole crab specimens show body pitching of

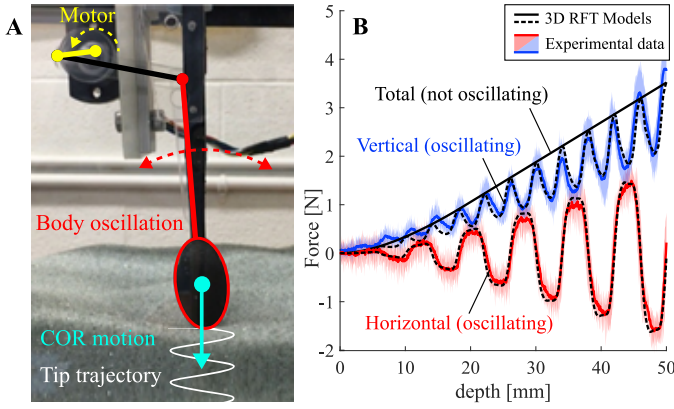


Fig. 7. **Pacific mole crab-inspired oscillations.** (A) The experimental setup consists of a motorized linkage mechanism that produces oscillation in body pitch about the indicated center of rotation (COR) at the desired amplitude and frequency during penetration. Tip trajectory is indicated with a gray line. The planar trajectory of the ellipsoid tip occurs at a frequency of 1.25 Hz and amplitude of  $\sim 9$  degrees. (B) Model-predicted vertical and lateral forces (dashed black curves) acting on the oscillating body throughout intrusion are compared with experimentally-obtained results for an identical experimental burrowing trajectory. Experimental lateral force (red) and vertical force (blue) represent means over 5 experimental trials. The shaded areas indicate mean and  $\pm$  standard deviation of experimental results. The force response predicted by the model of the intruding ellipsoid without oscillations is also compared with the oscillation data.

the crabs at a frequency of 1-2 Hz and magnitudes of 2-10° during burrowing events. The present work is not intended to provide biomechanical or morphological assertions about this organism; we mimic this observed motion to constrain our simulation to biologically-relevant motion scales and compare our robotic experimental data with simulation results.

The shape of the mole crab is simplified to a 3D printed ellipsoid with an aspect ratio matching that observed in animals (36mm height x 19mm width/depth). During insertion trials, the ellipsoid oscillates about a horizontal axis, representing the intersection of the animals' transverse and frontal planes at approximately the center of mass. A set of linkages is utilized to create the desired oscillations and is driven from above by a DC motor, shown in Fig. 7(A). In experiments, the ellipsoid mechanism is fixtured to a vertically-oriented bar with 0.4 cm<sup>2</sup> cross-sectional area, which is not accounted for in simulation. This discrepancy may account for some error in model predictions. Experiments are performed at the same frequency, amplitude, and intrusion velocity as in simulation: frequency 1.25 Hz, amplitude 9 degrees and downward vertical velocity 5 mm/sec.

We compare the vertical and lateral forces averaged over five experimental trials with model-predicted values, with results in Fig. 7(B) indicating overall agreement. The lateral force oscillates about zero with half the frequency of vertical force oscillations because peaks in vertical force occur when the lateral force passes a value of 0 N. The oscillating ellipsoid changes direction at these points, thus vertical resistive forces dominate when there is no lateral velocity. Irregularities in the substrate's surface, such as small mounds or holes, alter shallow intrusion forces and make depth measurements less precise, thus we have aligned the peaks in measured lateral

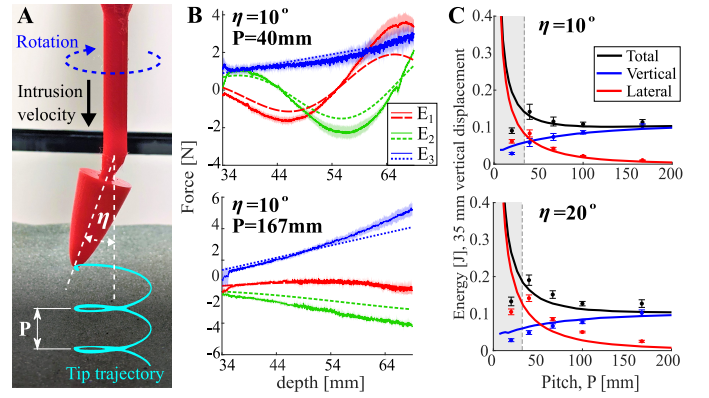


Fig. 8. **Root-inspired circumnutation.** (A) A root-inspired penetrator performs tip circumnutation while inserted vertically into soil. Directions of penetrator rotation, intrusion velocity, and trip trajectories are indicated. Tip angle is defined as  $\eta$ , and vertical distance traveled in one rotation is defined as pitch  $P$ . The 3D circumnutation trajectory of the root tip has a fixed period of 24 seconds and varying intrusion velocity in order to vary the overall circumnutation rate. (B) For a single value of tip angle  $\eta$  and two different rotation rates  $P$ , resistive forces are compared between simulation and experiment. Solid lines represent experimental means over three trials and shaded regions represents standard deviation. Dashed lines indicate model predictions. (C) For two different values of tip angle  $\eta$ , energy consumption required for a 35 mm vertical displacement is compared between simulation and experiment. Solid lines represent results from RFT-based simulation, while dots represent means of experimental data and error bars represent standard deviation over three trials. The grayed region left of dashed line indicates where substrate re-interaction is expected.

force to adjust for phase lag and depth discrepancies upon initial intrusion.

The results of this data suggest that oscillation at this frequency and amplitude results in transient reductions in the vertical force component. However, the peak vertical forces are unchanged compared with the non-oscillating case, and there is an energetic cost to oscillate the body because of the large lateral forces required. Independent of these specific observations, this experiment stands as an example of how RFT can be computed for a curved 3D object over a complex planar trajectory using the proposed method, which can help to motivate further study into new robot control strategies.

#### D. Parametric study of circumnutation

Circumnutation is a 3D intrusion strategy studied extensively in the context of root penetration [2], [27] and used in robot design and control [31]. The benefits of circumnutation to root penetration are not yet fully understood, though evidence indicates multifunctionality, including obstacle avoidance and robustness to a variety of substrates [32]. Recent empirical results by Del Dottore et al. (2017), using a robotic testbed, indicate an energetic advantage to circumnutation relative to straight vertical penetration.

We explore this phenomena in dry, uniform granular media using the aforementioned UR robot and MATLAB simulation. A root-inspired paraboloid probe holds a fixed angle  $\eta$  relative to the vertical penetration direction, which the probe is also rotated about. This results in a helical tip trajectory with a pitch of  $P$ , as shown in Fig. 8(A). The paraboloid is first inserted to a depth such that it is below the surface, then

inserted with circumnutation for an additional 35 mm of depth. In the experimental setup, the angular velocity of the robot wrist is held constant at  $15^\circ/\text{sec}$  and the pitch of the helical path is controlled via vertical intrusion velocity. The thin vertical rectangular body to which the root tip is fixtured is not accounted for in simulation.

Measured and simulated forces for  $\eta=10^\circ$  and  $P=[40,167]$  mm are shown in Fig. 8(B). We also compare the energy required to reach 35 mm depth across varying helical pitch lengths for  $\eta = [10^\circ, 20^\circ]$ , shown in Fig. 8(C); results match trends found in [27]. For  $P \geq 40$  mm, there is agreement between the model and the measured vertical insertion energy; however, force predictions deviate for  $P=20$  mm. The shaded region indicates when the trajectory of the root tip intersects its own path. Intrusion introduces both surface disturbances and changes in grain packing, which likely increase as pitch reduces and material re-interaction occurs.

## V. DISCUSSION

Velocity decomposition provides a method for implementing 3D RFT models that utilize data collected from orthogonal horizontal and vertical planes alone, through the characterization of terms  $f_1$  and  $f_{23}$ . However, this approach assumes an  $\alpha_y$  function, which in this work is selected as  $\alpha_y = \alpha_x (\gamma=0, \beta=0)$ . In order to reduce error further, a more complex empirical model for this resistive coefficient can be characterized using data outside of the two horizontal and vertical planes of motion. Future work will investigate whether a an empirical model for  $\alpha_y(\gamma, \beta)$  can be scaled to different granular materials for use in 3D, as demonstrated for 2D RFT [14]. The current work shows that assuming a simple model for  $\alpha_y$  can be useful, but this implementation will be more or less accurate for different shapes and trajectories.

The geometries analyzed in this study are symmetric convex hulls, for which the majority of discretized elements have intermediate values of  $\beta$ . Because error is demonstrated to be lower for these intermediate values, the model is expected to perform well in these scenarios. While we expect this simulation method to generalize to more irregular geometries, future work should investigate application to asymmetric 3D shapes and shapes with concave features, which are known to affect 2D granular RFT accuracy. Also note that the discontinuity in the orientation of  $\mathbf{e}_1$  as  $\beta$  approaches  $0^\circ$ , defined in Sec. II, has the potential to introduce simulation inconsistency for bodies and motions which contain many elements with low  $\beta$ . These effects will be explored in future work.

### A. Computation time & spatial convergence

3D RFT simulation times increase approximately linearly with the number of body plate elements,  $n$ , for a given time step and thus are dependent on body discretization mesh density. The force on each plate element requires several algebraic operations to compute. Fewer calculations are performed by either decreasing the number of plate elements or increasing the time step size,  $\Delta t$ . The simulation parameters utilized to generate Figs. 7 and 8 are reported in Fig. 9(A), along with computation times.

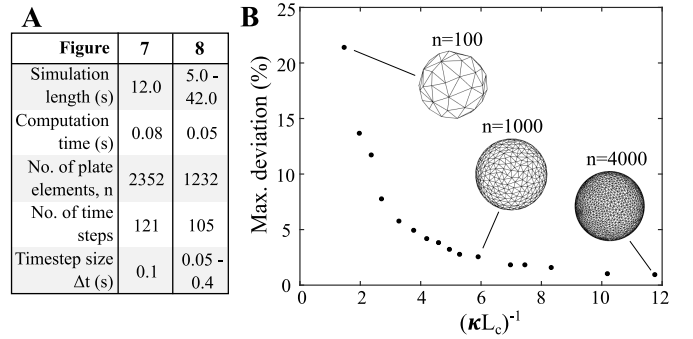


Fig. 9. **The effect of meshing resolution.** (A) The parameters utilized to simulate the results in Figs. 7 and 8 are reported along with computation times for the adopted personal computer (2.6GHz 6-core Intel Core i7, Turbo Boost up to 4.3GHz, with 9MB shared L3 cache). (B) Dimensionless parameter  $(\kappa L_c)^{-1}$  describes the characteristic length of the mesh element size  $L_c$  relative to the curvature  $\kappa$ . Spherical meshes are generated using Autodesk Meshmixer. The MATLAB Global Optimization Toolbox is used to compute the maximum and minimum resistive force magnitudes over all mesh orientations; the reported deviation is the percent difference.

In order to analyze the effect of element density on the precision of 3D RFT, a spherical body is meshed into .STL files of varying numbers of triangular elements,  $n$ . Resistive forces are calculated as the sphere is translated in the  $\mathbf{E}_1$ - $\mathbf{E}_2$  plane and its orientation is varied. For each mesh, the difference between the maximum and minimum horizontal force magnitude over all possible orientations is reported in Fig. 9(B). Mesh density is characterized by the dimensionless parameter  $(\kappa L_c)^{-1}$ , where curvature  $\kappa$  is the inverse of the sphere radius and  $L_c$  is the characteristic length scale of the plate elements. In other words, a sphere of any radius requires the same number of elements to ensure convergence. At higher spatial resolutions or with a greater number of elements, deviation converges towards zero and the force is less sensitive to object orientation. For instance,  $(\kappa L_c)^{-1} = 6$  requires 1000 plate elements and reduces output force variation to 2.5%, which may be an appropriate balance between model fidelity and computation time.

Fast simulations create new opportunities to quickly compare machine control and design strategies through large parameter searches. Continued development of rapid simulation tools, like 3D granular RFT, will further empower the development of new robots and devices that can aptly interact with granular media. This 3D RFT tool is not intended to provide perfectly precise force predictions, but rather can rapidly provide insights and guidelines for comparing different robot control and mechanism design options. Thus, it complements more computationally intensive, high fidelity tools such as Discrete Element Method.

## VI. CONCLUSION

This work demonstrates how a 3D granular RFT method can be implemented in robot control applications for curved 3D shapes and arbitrary velocity directions. We provide a methodological approach for achieving this by utilizing projection of velocities. Conveniently, it is only dependent on a limited set of scaling factor characterizations and one additional plate

orientation parameter, yet can be used for a range of objects and trajectories. We expect this 3D extension of RFT to further expand the employment of granular RFT to broader applications, such as the design of mechanisms that interact with regolith, industrial machines that work with powders, or food service robots that handle grains.

#### ACKNOWLEDGEMENT

Prof. Robert Full and Ben McInroe, of the Dept. of Integrative Biology at the University of California at Berkeley assisted in collecting motion data for two mole crab specimens and provided feedback on the manuscript. Andras Karsai in Prof. Daniel Goldman's group at Georgia Tech provided MATLAB functions for RFT calculation based on their previous work in 2D RFT. L.K.T. conducted the experiments and relevant modelling. L.K.T, C.C. and H.S.S. prepared the manuscript. The authors have no competing interests.

#### REFERENCES

- [1] A. G. Winter, V. R. L. H. Deits, D. S. Dorsch, A. H. Slocum, and A. E. Hosoi, "Razor clam to RoboClam: burrowing drag reduction mechanisms and their robotic adaptation," *Bioinspiration & Biomimetics*, vol. 9, no. 3, p. 036009, 2014.
- [2] E. Del Dottore, A. Mondini, A. Sadeghi, V. Mattoli, and B. Mazzolai, "Circumnutations as a penetration strategy in a plant-root-inspired robot," in *2016 IEEE International Conference on Robotics and Automation (ICRA)*, 2016, pp. 4722–4728.
- [3] N. D. Naclerio, C. M. Hubicki, Y. O. Aydin, D. I. Goldman, and E. W. Hawkes, "Soft robotic burrowing device with tip-extension and granular fluidization," in *2018 IEEE/RSJ International Conference on Intelligent Robots and Systems (IROS)*, pp. 5918–5923.
- [4] R. Maladen, Y. Ding, P. Umbanhowar, and D. Goldman, "Undulatory swimming in sand: Experimental and simulation studies of a robotic sandfish," *I. J. Robotic Res.*, vol. 30, pp. 793–805, 2011.
- [5] R. D. Maladen, Y. Ding, C. Li, and D. I. Goldman, "Undulatory swimming in sand: Subsurface locomotion of the sandfish lizard," *Science*, vol. 325, no. 5938, pp. 314–318, 2009.
- [6] J. Tao, S. Huang, and Y. Tang, "Bioinspired self-burrowing-out robot in dry sand," *Journal of Geotechnical and Geoenvironmental Engineering*, vol. 145, no. 12, p. 02819002, 2019.
- [7] A. Martinez, J. DeJong, I. Akin, A. Aleali, C. Arson, J. Atkinson, P. Bandini, T. Baser, R. Borela, R. Boulanger, M. Burrall, Y. Chen, C. Collins, D. Cortes, S. Dai, T. DeJong, E. Del Dottore, K. Dorgan, R. Fragaszy, J. D. Frost, R. Full, M. Ghayoomi, D. Goldman, N. Gravish, I. Guzman, J. Hambleton, E. Hawkes, M. Helms, D. Hu, L. Huang, S. Huang, C. Hunt, D. Irschick, H. Lin, B. Lingwall, A. Marr, B. Mazzolai, B. McInroe, T. Murthy, K. O'Hara, M. Porter, S. Sadek, M. Sanchez, C. Santamarina, L. Shao, J. Sharp, H. Stuart, H. Stutz, A. Summers, J. Tao, M. Tolley, L. Treers, K. Turnbull, R. Valdes, L. V. Passen, G. Viggiani, D. Wilson, W. Wu, X. Yu, and J. Zheng, "Bio-inspired geotechnical engineering: Principles, current work, opportunities and challenges," *Geotechnique (In press)*, 2021.
- [8] S. S. Sharpe, Y. Ding, and D. I. Goldman, "Environmental interaction influences muscle activation strategy during sand-swimming in the sandfish lizard *scincus scincus*," *Journal of Experimental Biology*, vol. 216, no. 2, pp. 260–274, 2013.
- [9] H. Marvi, C. Gong, N. Gravish, H. Astley, M. Travers, R. L. Hatton, J. R. Mendelson, H. Choset, D. L. Hu, and D. I. Goldman, "Sidewinding with minimal slip: Snake and robot ascent of sandy slopes," *Science*, vol. 346, no. 6206, pp. 224–229, 2014.
- [10] A. G. Winter and A. E. Hosoi, "Identification and evaluation of the atlantic razor clam (*ensis directus*) for biologically inspired subsea burrowing systems," *Integrative and comparative biology*, 2011.
- [11] S. Huang and J. Tao, "Modeling clam-inspired burrowing in dry sand using cavity expansion theory and DEM," *Acta Geotechnica*, 2020.
- [12] J. Gray and G. J. Hancock, "The propulsion of sea-urchin spermatozoa," *Journal of Experimental Biology*, vol. 32, no. 4, pp. 802–814, 1955.
- [13] C. J. Brokaw, "Flagellar propulsion," *Journal of Experimental Biology*, vol. 209, no. 6, pp. 985–986, 2006.
- [14] C. Li, T. Zhang, and D. I. Goldman, "A terradynamics of legged locomotion on granular media," *Science*, vol. 339, no. 6126, pp. 1408–1412, 2013.
- [15] T. Zhang and D. Goldman, "The effectiveness of resistive force theory in granular locomotion," *Physics of Fluids*, vol. 26, 2014.
- [16] P. E. Schiebel, H. C. Astley, J. M. Rieser, S. Agarwal, C. Hubicki, A. M. Hubbard, K. Diaz, J. R. Mendelson III, K. Kamrin, and D. I. Goldman, "Mitigating memory effects during undulatory locomotion on hysteretic materials," *eLife*, vol. 9, p. e51412, 2020.
- [17] S. Agarwal, A. Karsai, D. Goldman, and K. Kamrin, "A generalized resistive force theory for rate-dependent intrusion phenomena in granular media," *arXiv:2005.10976 [cond-mat]*, 2020.
- [18] C. Li, S. T. Hsieh, and D. I. Goldman, "Multi-functional foot use during running in the zebra-tailed lizard (*callisaurus draconoides*)," *The Journal of Experimental Biology*, vol. 215, pp. 3293–3308, 2012.
- [19] K. Tsuchiya and G. Ishigami, "Experimental analysis of bucket-soil interaction mechanics using sensor-embedded bucket test apparatus," in *Proceedings of the 10th Asia-Pacific Conference of the ISTVS*, 2018.
- [20] S. Shrivastava, A. Karsai, Y. O. Aydin, R. Pettinger, W. Bluethmann, R. O. Ambrose, and D. I. Goldman, "Material remodeling and unconventional gaits facilitate locomotion of a robophysical rover over granular terrain," *Science Robotics*, vol. 5, no. 42, 2020.
- [21] J. Ghaboussi and R. Barbosa, "Three-dimensional discrete element method for granular materials," *International Journal for Numerical and Analytical Methods in Geomechanics*, vol. 14, no. 7, pp. 451–472, 1990.
- [22] P. A. Cundall and O. D. L. Strack, "A discrete numerical model for granular assemblies," *Géotechnique*, vol. 29, no. 1, pp. 47–65, 1979.
- [23] A. Khosravi, A. Martinez, J. DeJong, and D. Wilson, "Discrete element simulations of bio-inspired self-burrowing probes in sands of varying density," 2018.
- [24] Y. Chen, A. Khosravi, A. Martinez, J. DeJong, and D. Wilson, "Analysis of the self-penetration process of a bio-inspired in situ testing probe," *Geo-Congress 2020*, pp. 224–232, 2020.
- [25] S. Dunatunga and K. Kamrin, "Continuum modeling and simulation of granular flows through their many phases," *Journal of Fluid Mechanics*, vol. 779, pp. 483–513, 2015.
- [26] H. Askari and K. Kamrin, "Intrusion rheology in grains and other flowable materials," *Nature Materials*, vol. 15, no. 12, pp. 1274–1279, 2016.
- [27] E. Del Dottore, A. Mondini, A. Sadeghi, V. Mattoli, and B. Mazzolai, "An efficient soil penetration strategy for explorative robots inspired by plant root circumnavigation movements," *Bioinspiration & Biomimetics*, vol. 13, no. 1, p. 015003, 2017.
- [28] D. I. Goldman and D. L. Hu, "Wiggling through the world: The mechanics of slithering locomotion depend on the surroundings," *American Scientist*, vol. 98, no. 4, pp. 314–323, 2010.
- [29] K. Dorgan, C. Law, and G. Rouse, "Meandering worms: Mechanics of undulatory burrowing in muds," *Proceedings. Biological sciences / The Royal Society*, vol. 280, p. 20122948, 2013.
- [30] B. McInroe, T. Bolas, I. Ko, and R. Full, "Reconfigurable control modules enable rapid burrowing in a decapod crustacean," in *Society of Integrative and Comparative Biology Annual Meeting 2020*.
- [31] Y. Ozkan-Aydin, M. Murray-Cooper, E. Aydin, E. N. McCaskey, N. Naclerio, E. W. Hawkes, and D. I. Goldman, "Nutation aids heterogeneous substrate exploration in a robophysical root," in *2019 2nd IEEE International Conference on Soft Robotics (RoboSoft)*, pp. 172–177.
- [32] I. Taylor, K. Lehner, E. McCaskey, N. Nirmal, Y. Ozkan-Aydin, M. Murray-Cooper, R. Jain, E. W. Hawkes, P. C. Ronald, D. I. Goldman, and P. N. Benfey, "Mechanism and function of root circumnavigation," *bioRxiv*, p. 2020.05.04.075127, 2020.